A

500μm

F

B

h

C

(h)

D

E

h

G

H

I

(h)

J

h

lymphocytes and afferent veiled cells (Stoll et al. 2002), B lymphocytes and veiled cells (Dubois et al. 1999), and interdigitating dendritic cells and afferent antigens (Imai et al. 1998). Afferent veiled cells may transport cancer-related antigens from dendritic cell infiltration into the primary focus (Tsujitani et al. 1990; Tsuge et al. 2000), while clusters of T and B lymphocytes and dendritic cells (Creusot et al. 2002) appear to be easily formed when the surface area of the cortex is large and when the T and B lymphocyte-containing areas are intermingled. With these features in mind, during the present study we noted the basic architecture (i. e. the configuration and the relative proportions of the cortical and sinusoidal areas) of various lymph nodes. We then carried out a comparative histological study to characterize the histological architectural features of lymph nodes, especially of the cortex, from aged experimental animals and elderly humans in order to estimate any potential alterations in nodal function with aging in humans.

Materials and methods

Materials. Twelve submandibular, 14 axillary central, 44 thoracic (20 subcarinal and 24 pulmonary hilar), 50 abdominal (14 superior mesenteric, 15 paracolic and 21 paraaortic) and 9 inguinal lymph node specimens from a total of 129 nodes were obtained from 27 donated cadavers (12 men and 15 women) aged from 72 to 95 years at death. Only one node was collected from each site in a respective cadaver. The cadavers showed no macroscopic evidence of tumors and, according to their death certificates, none of them died from neoplasms. The most common cause of death was pneumonitis, according to the death certificates. All cadavers were fixed by arterial perfusion of 10% formalin solution 24–48 hours after death. Most of the human specimens used during the present study were also used in other recent studies (Sato et al. 2003; Taniguchi et al. 2003).

As morphometrical controls, 84 nodes were obtained from 14 aged experimental animals, i. e., 4 white rabbits (2 males and 2 females, aged 12–24 months), 4 guinea pigs (4 males aged 14 months), 2 Beagle dogs (2 males aged 8 years) and 4 Wistar rats (4 males aged 12–15 months). The animals had all been maintained under conventional feeding conditions, and were sacrificed by deep anesthesia with methylether before collection of the nodes. The sample nodes included 21 submandibular, 12 axillary, 7 pulmonary hilar or other thoracic (pulmonary-regional), 28 superior mesenteric, 4 lumbar or paraaortic and 12 inguinal nodes. Because the nodes were difficult to find in some animals and/or at some sites, one or more nodes (3 at most) were col-

lected from each site where nodes could be identified. The nodes were fixed by immersion in 10% formalin solution.

Aged mice were not included in the present study because of difficulty in identification of the small nodes, less than 3 mm in the maximum diameter, and because, in our preliminary work using conventional C57 black and Bulb C mice aged 4–5 months (unpublished data), few regional difference was found in the histological configuration (see also "*Study limitation*" in Discussion).

Sectioning. Paraffin-embedded specimens of the nodes were prepared using routine procedures, and 10 μm-thick serial sections of each complete specimen were cut. We marked two axes for 3-dimensional reconstruction according to a conventional method: briefly, each paraffin block specimen was prepared as a cube or rectangular block with right angles between all adjacent surfaces and, before de-paraffinization, the glass slide was marked on two of the corners using a sharp glass-cutter. Using these labels, we were able to precisely compare structures between slices, but PC-aided 3-dimensional reconstruction was not performed.

Staining. Most sections were stained with hematoxylin and eosin (HE). Immunohistochemistry was also performed on several of them. The primary antibodies used in the immunohistochemical evaluation were anti-CD3 monoclonal antibody as a T lymphocyte marker (DAKO A/S, Glostrup, Denmark) for all materials including the animal nodes due to its cross reaction between mammals, and anti-human CD68 monoclonal antibody as a macrophage marker (DAKO A/S) for the human nodes only. Counterstaining, if necessary, was performed with hematoxylin.

Morphometry. Using HE-stained sections, a morphometrical study of the cortex and medullary cord (i. e., all cortical areas) was performed on all 74 animal and 129 human nodes (see above). Two or three sections from each node were studied; these always included both the hilus and the largest section of all the serial sections of the node. Their images were contrast enhanced with picture processing software (Photoshop; Adbe, U.S.A.) and the cortex measured with the NIH image (http://rsb.info.nih.gov/nih-image/). Because of 3-dimensional observations using serial sections (see above), we assumed that the results obtained from two or three slices would be representative of the entire node and, in the present study, we roughly estimated the proportional cortical areas as all cortical areas/all nodal areas in two to three slices (henceforward referred to as the "proportional area"). The proportional area obtained from one of the two or three slices of a node was different from that obtained from another section through only peripheral parts of the node. However, the difference was limited to 20% of the minimum value. The average will be shown in the Results.

Terminology. To facilitate comparative discussion, the terminology for lymph nodes used in the present study is based on that used in human anatomy (Richter and Feyerabend 1991; Földi and Kubik 1993). In rats, rabbits and guinea pigs, we found the

---

◄   ◄

Fig. 1. Histology of lymph nodes from elderly humans and aged experimental animals.

The largest or nearly largest serial sections of submandibular (parts A–E) and superior mesenteric (parts F–J) nodes from rats (parts A and F), guinea pigs (parts B and G), rabbits (parts C and H), dogs (parts D and I) and humans (parts E and J). Hematoxylin and eosin (HE) stain. The secondary follicles (arrows in B–D, G and I) can be seen in nodes from guinea pigs, dogs and rabbits. The medullary cord is very thin in the animal nodes (arrowheads). Note the thin superficial cortex (arrows in J) and thick cord-like structures (arrowheads in J) in the human mesenteric node. A follicle can be seen close to the hilus in this node (asterisk in J). h, hilus; h in parentheses, site near hilus. All parts are shown at the same magnification: the scale bar in A indicates 500 μm.
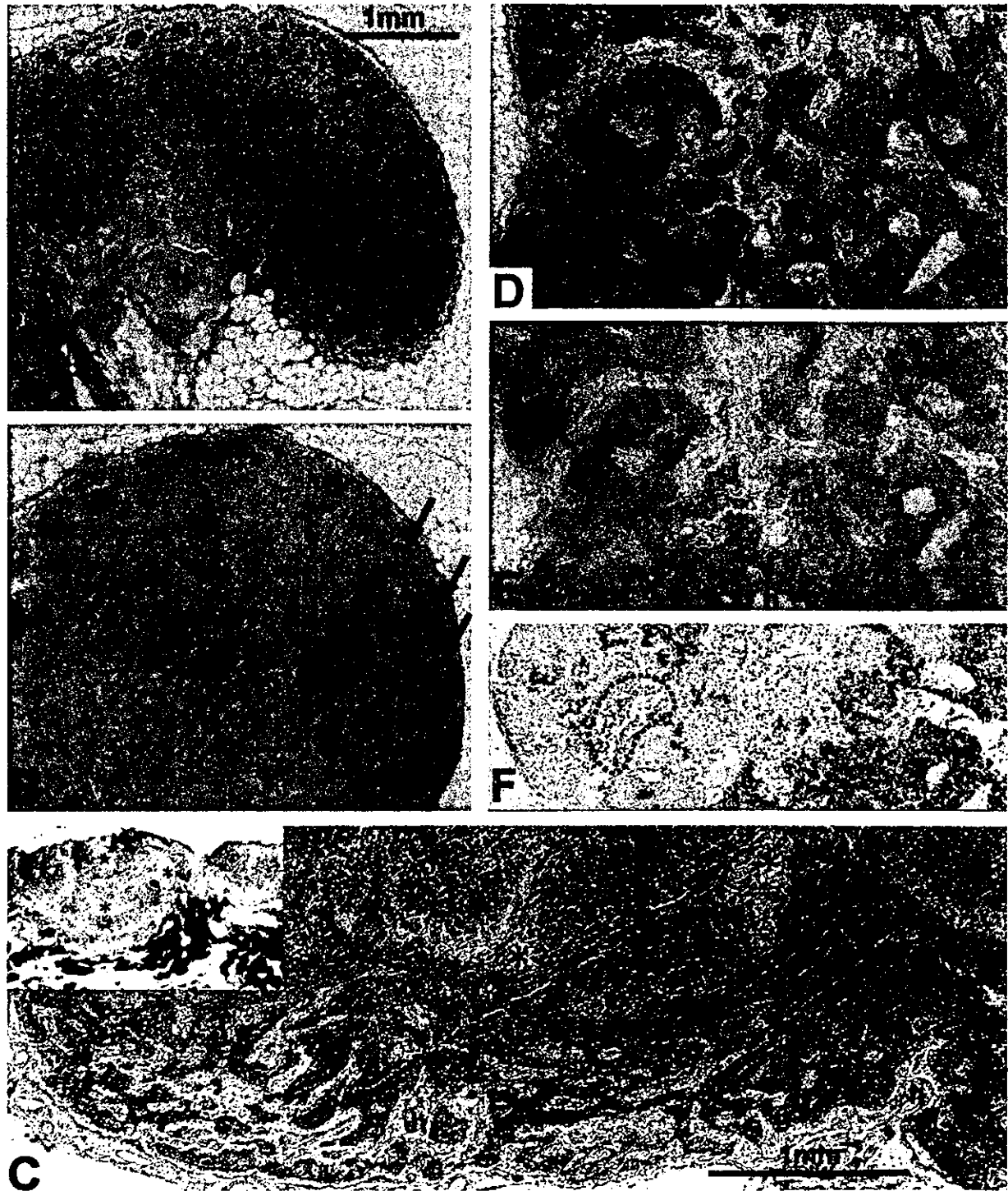
339

Fig. 2. Pulmonary regional nodes from a guinea pig, a dog and a human.

HE staining (parts A, C and D), CD3 (parts B and E and, an insert of part C) and CD68 (part F) immunohistochemistry. The upper four parts (A, B, and D-F) are shown at the same magnification (scale bar in part A, 1 mm). The pulmonary regional nodes of the guinea pig (parts A and B) have a sinus-rich architecture similar to those of humans (parts D-F). The medullary sinus of the guinea pig appears red because intranodal bleeding occured during dissection (part A). Part B shows a section almost 1 mm from that in part A (asterisks indicate the corresponding sites within the node according to a conventional reconstruction technique: see Materials and Methods). Severe anthracosis of the medullary sinusoidal macrophages is characteristic of the human node (parts D-F). In

axillary, inguinal and superior mesenteric node at sites corresponding to those in the human body. However, the thoracic nodes could not be identified as clearly as in humans (see the first paragraph of the Results). The nodes adjacent to the submandibular gland (i.e., the submaxillary nodes described by Greene 1955; the facial nodes by Tilney 1971) were termed the submandibular node, as in humans.

Ethics. The protocol for the present research project did not include any specific issue that needed to be approved by the Ethics Committees of our institutions. The present work conformed to the provisions of the declaration of Helsinki, 1964 (as revised in Washington 2002).
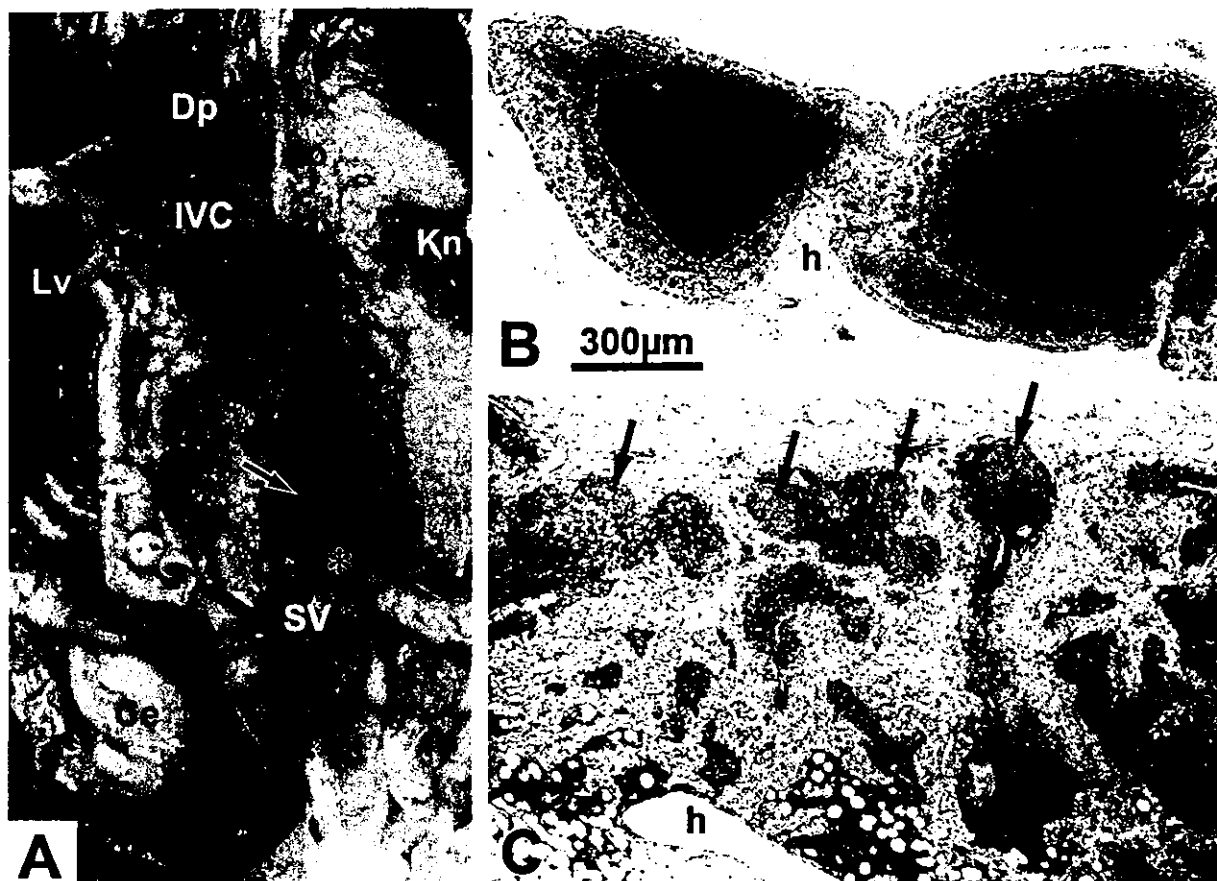

Fig. 3. Lumbar or paraaortic nodes from a rat and a human.

Part A shows the macroscopic dissection of a rat lumbar node. Ao, aorta; Ce, cecum; Dp, diaphragm; IVC, inferior vena cava; Kn, left kidney; LLN, lumbar lymph node; Lv, liver; Pr, prostate; Sv, seminal vesicle. The asterisks in part A indicate the corresponding parts of the cut rectum. Parts B and C illustrate the results of CD3 immunohistochemistry of the rat lumbar node (part B) and of the corresponding node in the human (the lower abdominal paraaortic node, part C). These are shown at the same magnification (scale bar in part B, 300 μm). The areas enclosed by dotted lines in part B and the arrows in part C indicate follicles or B lymphocyte-containing areas. Note the large aggregations of T lymphocytes in the rat node (part B) in contrast to the cord- or island-like configuration of the T cell-containing areas in the human node (part C). h, hilus.

◄

contrast, in the dog node, anthracotic cells are localized in the medullary cords and parts of cortices (part C). Note that the minute medullary cords of the guinea pig node (part B) contain few CD3-positive cells, in contrast to the thick cords of the human node (part E). The arrows in parts B and E indicate B lymphocyte-containing areas or follicles. For the dog node, a major color figure of part C is a higher maginification view of the inserted, black and white figure. B lymphocyte areas are indicated by a star and two asterisks in the insert and the asterisks correspond to those in a major figure of part C. h, hilus. Parts D-F show sections located very near to each other. Note the area enclosed by the dotted line in parts E and F, in which most of the CD68-positive cells are not accompanied by anthracosis.
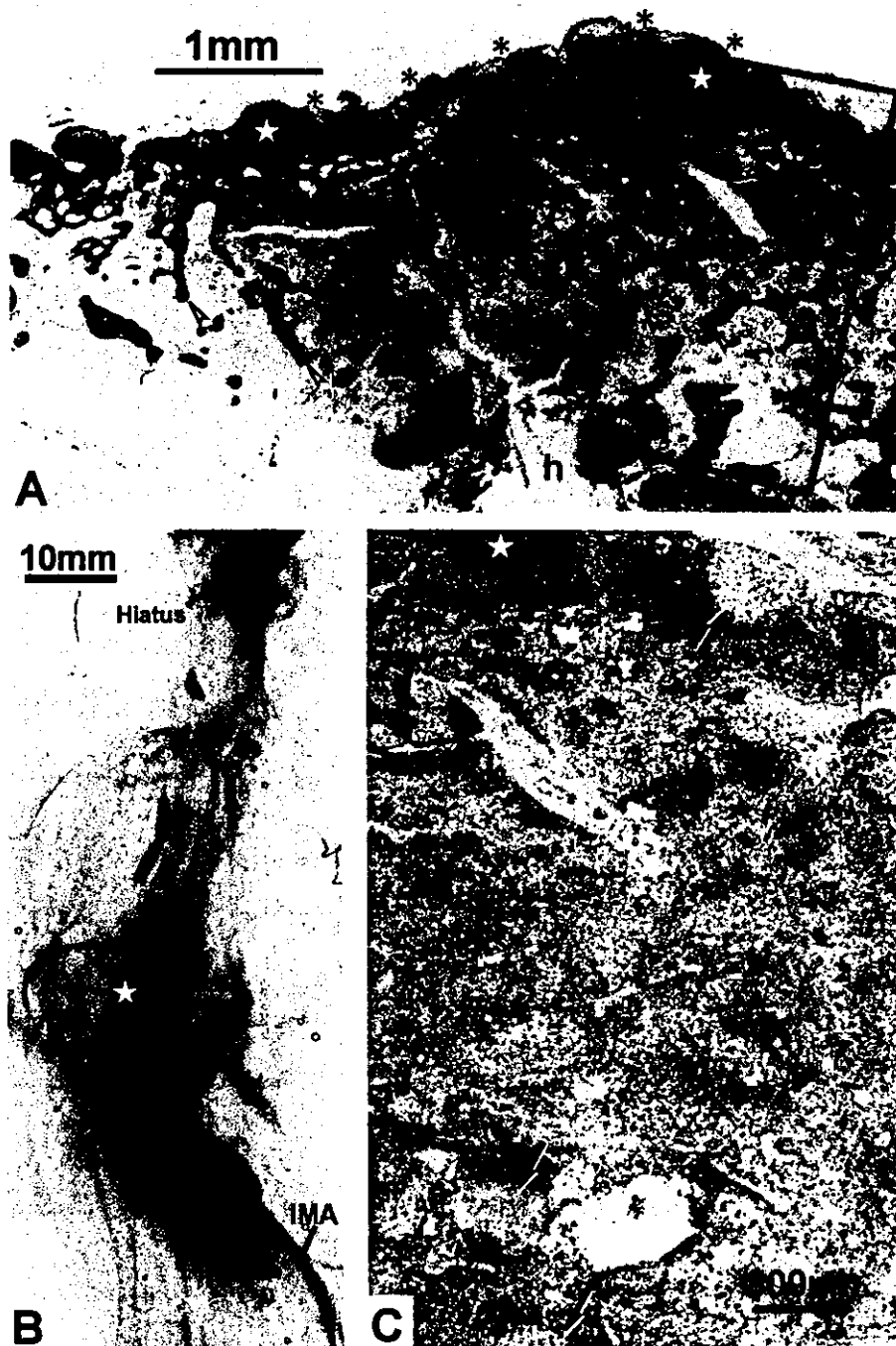
341

Fig. 4. Paraaortic nodes in dogs.

The dog paraaortic node (part A, HE staining) carries a superficial cortex layer in the afferent side (asterisks). However, darkly-stained follicle-like structures (white stars) do not correspond to B lymphocyte-containing areas (see also part C). h, hilus. The para-aortic nodes are large and multiple in number (part B; a specimen cleared in methyl salicylate). A node with a white star is histologically demonstrated in parts A and C; Hiatus, aortic hiatus of the diaphragm; IMA, inferior mesenteric artery. Part C (CD3 immuno-histochemistry) is a higher magnification view of a square in part A. One of the two white stars in part A corresponds to that in panel C. Arrows, follicles or B lymphocyte-containing areas. Scale bars in parts A, B and C indicate 1 mm, 10 mm or 300 µm, respectively.

342

Results

Gross observations. The pulmonary hilar node, which is well developed in humans, was not found at the hilum in rats or rabbits, but was located along the distal trachea and was very small. In these animals, this node seemed to correspond to the paratracheal, tracheobronchial and/or subcarinal node in humans. Thus, in this study, we chose the term "pulmonary regional nodes" rather than hilar node. Although the paraaortic node group always consisted of at least ten large, slender nodes in humans, we did not find any lymph nodes along the abdominal aorta or inferior vena cava in the three animal species examined except for dogs. The nearest equivalent in the rat seemed to be the lumbar node (Greene 1955; that was different from the iliac node in Tilney 1971), which was situated at the caudal angle of the aortic bifurcation or along the origin of the common iliac vessels.

Histology as determined by HE staining. In the lymph nodes of rats, guinea pigs, dogs and rabbits, the cortex could easily be discriminated from the medullary sinus (Fig. 1). The cortex issued numerous thin protrusions into the medullary sinus. These protrusions were identified as the medullary cord. However, the submandibular node of rats (Fig. 1 A) and the rabbit pulmonary hilar node (not shown) carried far fewer medullary cords, which were much shorter than those at the other sites. Thus, in these nodes, the cortical and sinusoidal areas tended to be clearly separated. No anthracotic macrophages were found in the pulmonary regional nodes of rats, rabbits, and guinea pigs. Although specific methods such as peanut agglutinin staining or an immune complex trapping assay (Horie et al. 1999) were not used, we were at least sometimes able to identify the germinal centers of the submandibular and superior mesenteric nodes of all four animal species by HE staining (Figs. 1 B–D, G and I). However, in rats and rabbits (especially rats), there were far fewer germinal centers per section than in guinea pigs and dogs. Guinea pig and dog nodes carried germinal centers at four of the five sites examined, the exception being the pulmonary hilar nodes. In guinea pigs, the maximum diameter of the secondary follicle in the inguinal and superior mesenteric nodes ranged from 300–400 μm, and these follicles were larger than those in the submandibular and axillary nodes (100–300 μm). Dog secondary follicles, 70–300 μm at the maximum diameter, were usually smaller than those of guinea pigs in the corresponding sites. Nevertheless, despite the above observations, regional differences in the nodes between the five sites examined in animals seemed to be less clear-cut than in humans (see below).

The human submandibular, axillary and inguinal nodes had a histological architecture similar to those of animals. Thus, they could be clearly divided into the cortical and medullary sinusoidal areas because of the prominent cortical area with small numbers of medullary cords seen in each section (Fig. 1 E). However, in human thoracic and abdominal nodes (i.e., the subcarinal, pulmonary hilar, superior mesenteric, paracolic and paraaortic nodes), the superficial cortex was often thin, sometimes even thinner than the maximum diameter of the follicle (Figs. 1–3). This feature was observed in all sections, including the largest section through the hilus. Because of the thin, fragmented cortex, the paracortex or deep cortex was often difficult to identify in these human nodes. Thus, especially in human abdominal nodes, a cord- or island-like arrangement of the cortical area was evident. Notably, germinal centers were rarely observed in nodes from elderly humans; among the 129 nodes examined, they were found in only two paracolic and two paraaortic nodes, (present in only two of the 27 cadavers; not shown in figures). The secondary follicles (maximum diameter 200–350 μm) were usually larger than the primary follicles or B lymphocyte clusters (150–250 μm) in each section.

The trabeculae were poorly developed in the rat, guinea pig and most human nodes. However, in rabbits and dogs, some nodes were divided into two or three parts by thick, fibrous trabeculae. Nevertheless, the cortices of the human paraaortic nodes were sometimes divided into small nodules, and each nodule was surrounded by thick fibrous tissue (not shown). This tissue did not, however, appear to correspond to real trabeculae separating the afferent drainage territories (Bélisle and Sainte-Marie 1981) because it was distributed randomly and independently of the afferent duct terminals along the subcapsular sinus.

In addition, numerous anthracotic macrophages were evident in the sinusoidal areas of the human thoracic nodes (Fig. 2 D). Some anthracotic cells were also present in the cortical areas. Notably, in dog pulmonary regional nodes, anthracotic cells were localized in the medullary cords and parts of cortices (Fig. 2 C). Nodal hyalinization, appearing as a glassy, eosinophilic deposit, was sometimes seen in the human thoracic and paraaortic nodes (not shown in figures; details described in Taniguchi et al. 2003). In contrast, we found no nodal hyalinization in the four animal species examined.

Immunohistochemistry. On CD3 immunohistochemistry, the follicles were revealed as round areas with relatively poor staining (Fig. 2). These corresponded to the follicles identified by HE staining except for those in dogs (see the last sentence of this subsection). Notably, in guinea pigs, dogs and humans, primary follicles or B lymphocyte clusters were located not only in the superficial cortex but also in the medullary cord, although the cord faced the medullary sinus rather than the subcapsular sinus. The cord- or island-like cortical areas in the human nodes contained numerous CD3-positive cells, whereas few positive cells were found in the minute medullary cord of the animal nodes (Fig. 2 B). This difference in histological configuration was most evident between the human paraaortic node and the rat lumbar node, even though these sites were similar. In the rat lumbar node, CD3-positive cells formed centrally and/or superficially located clusters

343

or cores (Fig. 3 B), whereas in the human cortical areas they occurred in a cord- or island-like configuration that included follicles (Fig. 3 C). Dog paraaortic nodes were somewhat similar to humans because of thin cortical areas, thick medullary cords and rich sinusoidal areas (Fig. 4 A). However, in dogs, the afferently-sided superficial cortex was not fragmented but formed a continuous sheet facing the afferent side of the node. Notably, CD3-positive cells formed follicle-like clusters in the dog superficial cortex as well as in the deep cortex (Figs. 4 A and 4 C).

CD68 immunohistochemistry of the human pulmonary regional nodes showed that positive cells were not usually anthracotic, especially when the macrophages were located away from the hilus (Figs. 2 D and 2 E). Anthracotic cells in both the cortical and sinusoidal areas were also CD68 positive. In human abdominal nodes, CD68 positive cells tended to surround each of the island-like cortical areas (figures, not shown).

Proportional area of the cortical area. The cortex and medullary cord, i. e., the area in which lymphocytes accumu-

lated, usually occupied 70–90% of the total nodal area in rats, rabbits, dogs and guinea pigs (Fig. 5). However, the proportional area of the cortex tended to be small in the pulmonary regional nodes, although few nodes were examined because of difficulty in finding them. Interindividual variations were evident in the human as well as the animal nodes. Nevertheless, the proportional area of the cortices of the submandibular and inguinal nodes tended to be relatively large in animals. Moreover, in the human nodes, we found clear region-specific differences in the proportional area (Fig. 6). The human pulmonary hilar and subcarinal nodes had a small proportional cortical area (almost 30%), whereas a large proportional area tended to be found in the submandibular, inguinal, axillary and superior mesenteric nodes. In particular, in the first two of these sites, the cortical area always occupied more than 80% of the node, and this was consistent with nodes from the corresponding sites in animals except for
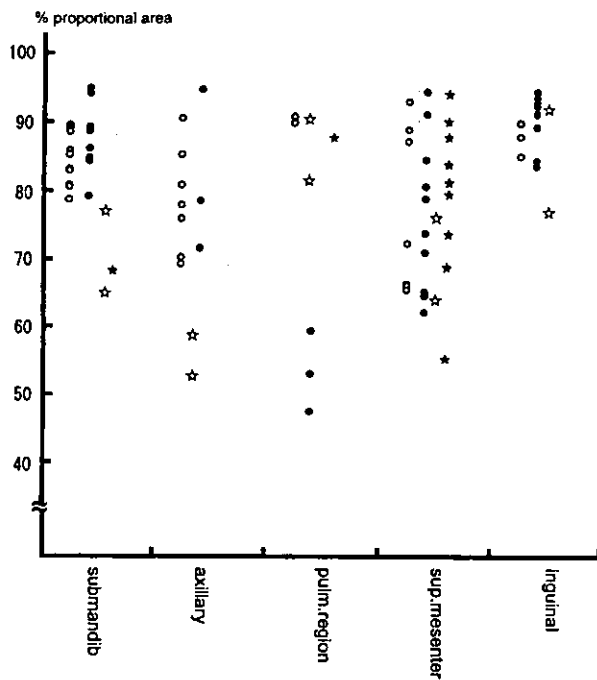

Fig. 5. Proportional areas of the cortical areas in nodes from guinea pigs, rats and rabbits.

The figure shows five columnar sets of labels, which indicate the proportional areas of the nodal cortices (%, y-axis) in the submandibular (submandib), axillary, pulmonary regional (pulm.region), superior mesenteric (sup.mesenter) and inguinal node groups, respectively. The black circles represent the guinea pig, the open circles represent the rat, the black stars represent the rabbit and, the open stars represent the dog. Lack of or smaller number of the labels within some columns (as seen for the pulmonary regional nodes), indicate that the node could not be or was only rarely found.
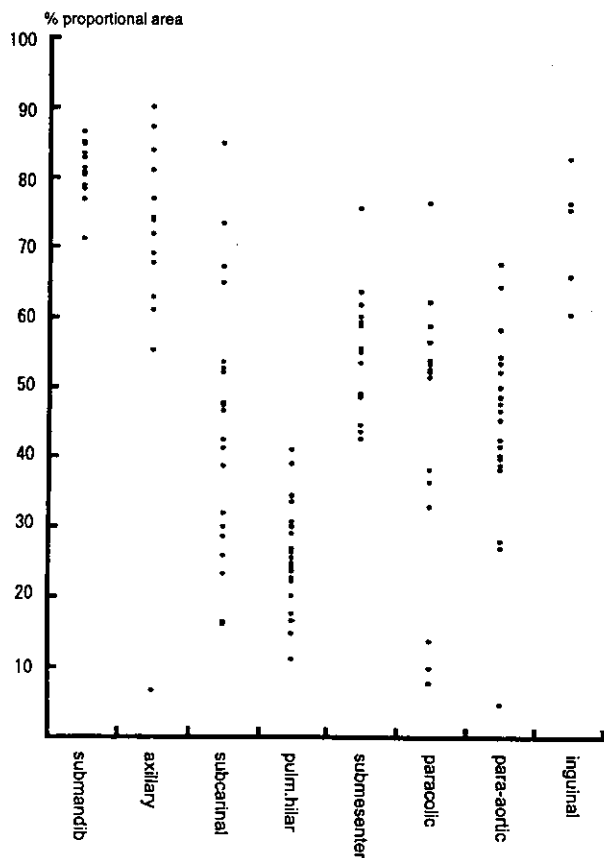

Fig. 6. Proportional areas of the cortical areas in human nodes.

Each of the eight sets of labels indicates the proportional areas of the nodal cortices (%, y-axis) in the submandibular (submandib), axillary, subcarinal, pulmonary hilar (pulm.hilar), superior mesenteric (sup.mesenter), paracolic, paraaortic and inguinal node groups, respectively. Discordance of the number of labels in each column (as seen for the inguinal node group) indicates small interindividual variation found during the first step of the present observations.

344

dog axillary nodes in which very thin medullary cords occupied in the large sinus area.

Although there were sufficient human specimens to allow statistical analysis, no intersexual differences in morphometry were evident because of relatively small numbers of specimens and because of the great interindividual variation.

Discussion

Although the numbers of species examined were limited, the present study demonstrated species-specific and region-specific differences in the histological configurations of lymph nodes from aged animals and humans, especially with respect to the histology of the lymphocyte-accumulating area, i.e., the cortex and medullary cord. Regional differences were evident between two main groups of sites; one group included the submandibular, axillary and inguinal nodes, while the other comprised the thoracic and abdominal nodes. The present two groups of nodes seemed to correspond to the somatic and visceral node classifications by Tilney (1971) and Hoshi et al. (2001). Notably, the differences between the two groups of nodes were more evident in humans than in the four animal species examined. In the human, most abdominal nodes were characterized both by the smaller proportional areas of their cortical areas and by the thin or island-like cortex. Thus, the afferently-sided, superficial cortex became similar to parts of the medullary cord. Gretz et al. (2000) suggested that lymph-borne cytokine transportation from the subcapsular sinus to the high endothelial venule was facilitated by thin superficial cortices. Among the animal nodes examined, the pulmonary regional node of the guinea pig was an exception, in that it had a relatively narrow, thin cortex with numerous, minute medullary cords. However, the guinea pig medullary cord contained few CD3-positive cells, in contrast to the human node.

These observations raise the questions of why such differences between the somatic and visceral node groups occur, and why these differences are more evident in human nodes. Horie et al. (1999) experimentally demonstrated that rapid numerical and volumetric alterations in follicles are caused by stimulants administered to the afferent side of the node. Conversely, long-term stimulation by different antigens in humans was most likely to cause changes and fixation of differences in the histological configuration. The functions of the human colon and cecum seem to be quite different from those of animals in several respects, including antigen presentation. Also in contrast to the animal nodes except for dog nodes, the human pulmonary hilar and subcarinal nodes were markedly characterized by anthracotic macrophages and small cortical proportional areas. Notably, the human subcarinal node, in which the lymph flow from the esophagus joins the lymph drainage of the lower lung lobe (Richter and Feyerabend 1991; Földi and Kubik 1993), showed the

second smallest proportional area overall, but with a large degree of interindividual variation. Thus, conversely, the pulmonary lymph flow may prohibit the maintenance of a large cortical proportional area in the human.

In the human, numerous large paraaortic nodes are situated alongside the abdominal aorta, including the aortic bifurcation (Richter and Feyerabend 1991; Földi and Kubik 1993). Dog paraaortic nodes were also multiple and large, but they did not form a nodal chain. In contrast, only one or two lumbar nodes were found at corresponding sites in another three animal species tested, although Crouch (1969) reported the lower abdominal paraaortic nodes to be well developed in the cat. In humans, the relatively short lumbar and intestinal lymph trunks drain into some of the paraaortic nodes, and these nodes in turn issue two or three roots of the thoracic duct. Conversely, the cisterna chyli is rather atypical in humans. Thus, human paraaortic nodes occupied a critical position as the last-intercalated node for metastasis of abdominal and pelvic solid neoplasms (Hirai et al. 2001; Murakami et al. 2002). In contrast, in animals, the long lumbar and intestinal trunks join to make the cisterna chyli from which the thoracic duct originates (Greene 1955; Crouch 1969; Miller 1969; Tilney 1971). The histology of the rat lumbar node, rich in cortical tissue, was quite different from that in humans (Fig. 3; see also below). Dog paraaortic nodes were rich in sinusoidal tissue, but the superficial cortex was not fragmented. These differences seemed to be related to the patterns of origin of the thoracic duct. In animals, it appears to be difficult for intestinal lymph to reach the lumbar node, even if lymph reflux occurs.

A cord- or island-like arrangement of the cortices was evident in almost all sections of human abdominal nodes, especially of the paraaortic nodes. This feature was not restricted to the area around the nodal hilus but occurred even in the afferent areas of the cortices. Although PC-aided reconstruction was not included in the present study, we recently demonstrated the 3-dimensional configuration (Sato et al. 2003). In contrast, in the animals examined, the medullary cord was so thin that it could be clearly discriminated from the thick superficial cortex. In the lymph nodes of the wallaby (Old and Deane 2002), pig (Hoshi et al. 1986) and bovine (Aijima et al. 1986), the cortex-like areas or nodules seem to be surrounded by a sinus-like area. However, in these animals, each nodule seemed to correspond to a single functional unit (Bélisle and Sainte-Marie 1981) and to receive afferent vessels independently. In contrast, in most human abdominal nodes, the island-like cortex or nodules are surrounded by the sinus-like area common for several afferent openings (Sato et al. 2003). Because of the intermingling of the lymphocyte-containing areas and because of the larger surfaces surrounded by the sinus, various critical cell-cell interactions between the cortical and sinusoidal components (see Introduction) appeared to be facilitated by the island-like cortical structures when compared with animal nodes.

345

Because the sentinel node procedure has become a standard component of world-wide surgical treatment of early solid neoplasms (see Introduction), allowing investigation of the cells involved and determination of at which stage of invasion metastatic cancer cells are eliminated or lodged in a node, as well as evaluation of which cytokines modulate the process, many institutes in Japan have begun to develop experimental models using animals. However, none of the researchers has so far taken species- and region-specific variations in lymph node histology into consideration. This is important since variation is likely to be age-dependent, or, strictly speaking, aging seems to enhance the degree of variation. Although the rat mesenteric node is an especially convenient site for research on sentinal nodes, the histological differences might be even more evident between relatively young rats, which are routinely used in experiments, and elderly people suffering from cancers. In our opinion, based on the present results, guinea pigs appear to be a much better animal model of thoracic and abdominal cancer metastasis in the elderly than rats.

Study limitation. A potential limitation of the present study hinges on whether the body of an elderly (70 to 90-year-old) human is accurately reflected by the animals used in the present study. The apparent histological differences between human and animal nodes, including the low proportional area of the cortical area in the human, might be due to the relatively "young" age of the animals used.

Mice are the most popular experimental animals, but they were not included in the present study (see also Materials and methods). According to our preliminary studies using immunohistochemistry, the histology was usually composed of the peripherally-located B-lymphocyte areas, including a few primary follicle, and the centrally-located T-lymphocyte clusters. It was similar to the present observations of rat submandibular and lumbar nodes (Figs. 1 A and 3 B).

References

Aijima H, Horie K, Nagata H, Hoshi H (1986) Cortical structure of bovine lymph nodes. Acta Anat Nippon 61: 173–185

Bélisle C, Sainte-Marie G (1981) Tridimensional study of the deep cortex of the rat lymph node. I. Topography of the deep cortex. II. Relation of deep cortex units to afferent lymphatic vessels. Anat Rec 199: 45–59

Bourgeois P (2002) Effect of age and lateralization on lymphoscintigraphic interpretation. Nuclear Med Comm 23: 257–260

Creusot RJ, Mitchison NA, Terazzini NM (2002) The immunological synapse. Mol Immunol 38: 997–1002

Crouch JE (1969) Text-Atlas of Cat Anatomy. Lea & Febiger, Philadelphia

Delemarre FGA, Kors N, Kraal G, van Rooijen N (1990 a) Elimination of spleen and of lymph node macrophages and its difference in the effect on the immune response to particulate antigens. Immunobiology 182: 70–78

Delemarre FGA, Kors N, Kraal G, van Rooijen N (1990 b) Repopulation of macrophages in popliteal lymph nodes of mice after liposome-mediated depletion. J Leukocyte Biol 47: 251–257

Dubois B, Barthélémy C, Durand I, Liu YJ, Caux C, Brière F (1999) Toward a role of dendritic cells in the germinal center reaction: triggering of B cell proliferation and isotype switching. J Immunol 162: 3428–3436

Faries MB, Bedrosian I, Reynolds C, Nguyen HQ, Alavi A, Czerniecki BJ (2000) Active macromolecule uptake by lymph node antigen-presenting cells: a novel mechanism in determining sentinel lymph node status. Ann Surg Oncol 7: 98–105

Földi M, Kubik S (1993) Lehrbuch der Lymphologie. 3. Auflage. Gustav Fischer, Stuttgart

Geijtenbeek TB, Groot PC, Nolte MA, van Vliet SJ, Gangaram-Panday ST, van Duijnhoven GC, Kraal G, van Oosterhout AJ, van Kooyk Y (2002) Marginal zone macrophages express a murine homologue of DC-SIGN that captures blood-borne antigens in vivo. Blood 100: 2908–2916

Greene EC (1955) Anatomy of the Rat. Hafner Publishing Co., New York

Gretz JE, Norbury CC, Anderson AO, Proudfoot AEI, Shaw S (2000) Lymph-borne chemokines and other low molecular weight molecules reach high endothelial venules via specialized conduits while a functional barrier limits access to the lymphocyte microenvironments in lymph node cortex. J Exp Med 192: 1425–1440

Hirai I, Murakami G, Kimura W (2001) Origins of the thoracic duct: a gross anatomical study based on the general classification of lymph node in Japan. J Hep Bil Pancr Surg 8: 441–448

Horie K, Chen D, Hoshi H (1999) Development of immune complex trapping: experimental study of lymphoid follicles and germinal centers newly induced by exogenous stimulants in mouse popliteal lymph node. Histol Histopath 14: 11–21

Hoshi N, Hashimoto Y, Kitagawa H, Kon Y, Kudo N (1986) Histological and immunological studies of the architecture of lymph nodes in pig. Jpn J Vet Sci 48: 1097–1107

Hoshi H, Horie K, Tanaka K et al. (2001) Patterns of age-dependent changes in the numbers of lymph follicles and germinal centers in somatic and mesenteric lymph nodes in growing C57B1/6 mice. J Anat 198: 189–205

Imai Y, Yamakawa M, Kasajima T (1998) The lymphocyte-dendritic cell system. Histol Histopath 13: 469–510

Kitagawa Y, Fujii H, Mukai M, Kubota T, Ando N, Watanabe M, Ohgami M, Otani Y, Ozawa S, Hasegawa H, Furukawa T, Kumai K, Ikeda T, Makahara T, Kubo A, Kitajima M (2000) The role of the sentinel lymph node in gastrointestinal cancer. Surg Clinics North Am 80: 1799–1809

Miller ME (1969) Anatomy of the Dog. Saunders, Philadelphia

Murakami G, Abe M, Abe T (2002) Last-intercalated node and direct lymphatic drainage into the thoracic duct from the thoracoabdominal viscera. Jpn J Thorac Cardiovasc Surg 50: 93–103

Old JM, Deane EM (2002) Immunohistochemistry of the lymphoid tissues of the tammar wallaby, Macropus eugenii. J Anat 201: 257–266

346

426

Richter E, Feyerabend T (1991) Normal Lymph Node Topography. Springer, Berlin

Rópolo A, Morón VG, Maletto B, Pistoresi-Palencia MC (2001) Diminished percentage of antigen bearing cells in the lymph nodes of immune aged rats. Exp Gerontol 36: 519–535

Sato A, Taniguchi I, Fujiwara D, Ichikawa H, Suzuki M, Nawata S, Murakami G (2003) Gaps and fragmentation of the superficial cortex in the abdominal and pelvic lymph nodes of elderly Japanese. Anat Sci Int 78: 211–222

Stoll S, Delon J,.Brotz TM, Germain RN (2002) Dynamic imaging of T cell-dendritic cell interactions in lymph nodes. Science 296: 1873–1876

Taniguchi I, Murakami G, Sato A, Fujiwara D, Ichikawa H, Yajima T, Kohama G (2003) Lymph node hyalinization in elderly Japanese. Histol Histopathol 18: 1169–1180

Tilney NL (1971) Patterns of lymphatic drainage in the adult laboratory rat. J Anat 109: 369–383

Tsuge T, Yamakawa M, Tsukamoto M (2000) Infiltrating dendritic/Langerhans cells in primary breast cancer. Breast Cancer Res Treat 59: 141–152

Tsujitani S, Kakeji Y, Watanabe A, Kohnoe S, Maehara Y, Sugimachi K (1990) Infiltration of dendritic cells in relation to tumor invasion and lymph node metastasis in human gastric cancer. Cancer 66: 2012–2016

van der Valk P, Meijer CJLM (1997) Reactive lymph node. In: Sternberg SS (Ed) Histology for Pathologists, 2nd ed. Lippincott-Raven, Philadelphia, pp. 651–673

van Rooijen N (1991) Antigen processing and presentation in vivo: the microenvironment as a crucial factor. Immunol Today 11: 436–479

Veronesi U, Paganelli G, Galimberti V, Viale G, Zurrida S, Bedoni M, Costa A, de Cicco C, Geraghty JG, Luini A, Sacchini V, Veronesi P (1997) Sentinel node biopsy to avoid axillary dissection in breast cancer with clinically negative lymph nodes. Lancet 349: 1864–1867

347

Increased Expression of the Genes for Mitotic Spindle Assembly and Chromosome Segregation in Both Lung and Pancreatic Carcinomas

KENJI HAMADA[1], MICHIO UEDA[3], MASAMI SATOH[2], NAOHITO INAGAKI[1], HIROSHI SHIMADA[3] and HISAFUMI YAMADA-OKABE[1]

[1]*Pharmaceutical Research Department IV, Kamakura Research Laboratories, Chugai Pharmaceutical Co. Ltd., 200 Kajiwara, Kamakura, Kanagawa 247-8530;* [2]*Department of Surgery, Tohoku University, 4-1 Seiryoucho, Aobaku, Sendai, Miyagi 980-8575;* [3]*Department of Surgery, School of Medicine, Yokohama City University, 3-9 Fukuura, Kanazawa, Yokohama, Kanagawa 236-0004, Japan*

Abstract. *Genes whose expression was modulated in two different tumor types, lung or pancreatic carcinoma, were identified by DNA microarray and subsequent expression correlation analyses. For more accurate comparison of the gene expression between tumor and normal cells, tumor cells and normal epithelium cells were isolated by laser-captured microdissection. Genes whose expression was significantly altered in lung carcinomas or pancreatic carcinomas as compared to their normal counterparts were ranked by the T-values calculated from the Fisher's ratios and their corresponding background Fisher's ratios, followed by statistical confirmation using the Welch's t-test. Among the genes that were ranked in the top 150, either in lung carcinomas or pancreatic carcinomas, expressions of MAD2, BUB1, BUB1B, HEC, CENPE, ZWINT, KNSL1, SMC4, CCNB, TK and PMS2L6 were found to be significantly up-regulated in both tumor types. Interestingly, 8 of the above 11 genes code for the proteins involved in the mitotic spindle assembly and chromosome segregation. Furthermore, the search for genes whose expression correlated with one of the above 5 genes yielded additional genes that are also considered to be involved in mitotic spindle assembly and chromosome segregation. Thus, increased expression of the genes for mitotic spindle assembly and chromosome segregation are a common*

feature of at least lung carcinomas and pancreatic carcinomas and, therefore, such genes may be potential targets for widely effective anticancer agents.

Lung cancer and pancreatic cancer are among the most frequent causes of cancer death worldwide. Although new molecular-targeting drugs such as Iressa and Gemzar have been introduced into their treatment, the efficacy of chemotherapeutic agents against these cancers is still limited (1, 2). Since lung and pancreatic cancers are often asymptomatic in their early stages, most patients have widespread disease at the time of diagnosis. Genome-wide gene expression analysis by DNA microarray with surgical specimens has led to the identification of new sets of genes involved in the development and growth of tumors, metastasis, prognosis and sensitivity and resistance to drugs in many cancer types (3, 4).

DNA microarray is a powerful technique for comprehensive analysis of gene expression, though a method for extracting genes of interest from a large number of genes using a relatively small number of samples has not been well established. Previously, we adopted a combination of the Fisher's ratio and the leave-one-out method to analyze DNA microarray data and identified genes that were differentially expressed between HBV- and HCV-infected hepatocellular carcinomas (5, 6).

In an attempt to understand more about the fundamental molecular characteristics of lung and pancreatic cancers and to identify useful molecules for therapies and diagnosis across different tissue and tumor types, we analyzed the gene expression profiles of two different tumor types, lung carcinomas and pancreatic carcinomas, and compared the results with profiles of their normal counterparts.

Because of a higher percentage of stromal cells such as fibroblasts within lung and pancreatic tumor tissues, gene

Correspondence to: Hisafumi Yamada-Okabe, Pharmaceutical Research Department IV, Kamakura Research Laboratories, Chugai Pharmaceutical Co. Ltd., 200 Kajiwara, Kamakura, Kanagawa 247-8530, Japan.

231

expression profiling of these tumor tissues is rather complicated. To achieve an accurate comparison of the gene expression profiles of tumor and normal cells, cells in tumor tissues and their normal counterparts, *i.e.* normal epithelia of lung and pancreatic ducts, were isolated by laser-captured microdissection. For DNA microarray data analysis, T-values from Fisher's ratio and its corresponding background Fisher's ratio were applied to select genes whose expression was significantly altered in tumor tissues; the significance of the expression was statistically confirmed by Welch's *t*-test. By this gene selection procedure, we found that the expression of the 8 genes that are involved in spindle checkpoint and function during the metaphase to anaphase transition are up-regulated in both lung carcinomas and pancreatic carcinomas. Furthermore, a search for genes whose expression correlated with that of these 8 genes yielded additional genes responsible for mitotic spindle assembly and/or chromosome segregation. Thus, the altered expression of the genes for the metaphase to anaphase transition seems a common and important cellular response in tumor cells *in vivo*.

Materials and Methods

RNA isolation from microdissection sample. Samples of lung carcinoma and pancreas carcinoma were collected at Tohoku University Hospital and Yokohama City University Hospital, Japan, respectively. Written informed consent was obtained from all patients before surgery and the study protocol was approved by the Institutional Review Board for the Use of Human Subjects at each university. Tumor cells and non-tumorous normal cells were isolated by laser capture microdissection (model LM200, Arcturus, CA, USA). RNA isolation from microdissected samples was done with a Micro RNA Isolation Kit (Stratagene, CA, USA) according to the instruction manual.

cRNA synthesis and hybridization. Biotin-labeled cRNA was synthesized by two rounds of cDNA synthesis. In the first round, cDNA was synthesized from 20-50 ng of total RNA with 5 pmole of T7-promoter-linked (dT)-24 primer, 5'-GGCCAGTGAATTGTAA TACGACTCACTATAGGGAGGCGG-(T)24-3', in RT-buffer containing 0.5 mM dNTPs, 10mM DTT, 5mM MgCl$_2$ and 50 units of SuperScript II Reverse Transcriptase (Invitrogen, CA, USA) at 42°C for 1 h. Reverse strand cDNA was synthesized at 16°C for 2 h in a buffer containing 0.2mM dNTPs, 40 units of *E.coli* DNA polymerase, 1 unit of *E.coli* DNA ligase and 2 units of RNase H. Next, T4 DNA polymerase (10 units) was added to the reaction mixture and incubation was continued at 16°C for 5 min. The resulting cDNA was purified with Phase Lock Gel Light (Eppendorf, Germany), precipitated in ethanol and used as the template for cRNA synthesis. cRNA was synthesized with T7 RNA polymerase (MEGAscript, TX, USA) in a buffer containing 7.5mM of dNTPs at 37°C for 6 h, purified with RNeasy (QIAGEN, CA, USA), precipitated in ethanol and used as the template for the second round of synthesis. In the second round, cDNA was synthesized in a buffer containing all the cRNA synthesized in the first round, 1 µg of random hexamer (Invitrogen) 0.5 mM dNTPs, 10mM DTT, 5mM MgCl$_2$ and 50 units of SuperScript II RT at

25°C for 10 min followed by 50-min incubation at 42°C. RNase H (2 units) was then added to the reaction mixture and incubation was continued at 37°C for 20 min. After inactivation of RNase H at 95°C for 2 min, reverse strand cDNA was synthesized with the T7-promoter linked (dT)-24 primer at 16°C for 2h, purified with Phase Lock Gel Light, separated from the oligo-hexamer by QIAquick (QIAGEN), and precipitated in ethanol. The biotin-labeled cRNA was synthesized from the second round cDNA as a template. The cDNA was incubated in a buffer containing T7 RNA polymerase, 7.5 mM each of ATP, GTP and biotin-CTP, and biotin-UTP at 37°C for 6 h. The resulting cRNA was purified with RNeasy (QIAGEN) and precipitated in ethanol. This procedure yielded approximately 100 µg of biotin-labeled cRNA from 20-50 ng of total RNA. After confirming the quality of cRNA by electrophoresis, 30 µg of the cRNA was fragmented in a buffer containing 40 mM Tris-acetate, pH 8.1, 100mM KOAc and 30 mM MgOAc at 95°C for 35 min.

Ten micrograms of the fragmented cRNA were used for the hybridization with Affymetrix GeneChip®. Hybridization, washing, staining, amplification of the signals and scanning of the signals were carried out as described in previously (5, 6). The signal was calculated and normalized (global scaling by target intensity at 300) with Affymetrix Microarray Suite software (ver. 4.0).

Statistical analysis and selection using Fisher's ratio. Gene selection was carried out using a two-step selection procedure. Genes whose expression was significantly different between the two groups were selected according to the T-value calculated by Fisher's ratio and background Fisher's ratio (5,6), followed by statistical confirmation from Welch's *t*-test.

The Fisher's ratio for the jth gene was calculated by the formula:

$$F(j) = (\mu j(A) - \mu j(B))2/(P(A)\sigma - j^2(A) + P(B)\sigma - j^2(B))$$

where μj represents the mean value, $\sigma - j^2$ represents the variance, and P represents the number of the *a priori* probability. To reduce sampling error, Fisher's ratio was calculated for all $[_{nA}C_{nA-1} \times {}_{nB}C_{nB-1}]$ sample combinations generated by extracting one sample from each group (A and B); distributions of all sample combinations were determined.

Distribution was evaluated using the background Fisher's ratio that was calculated from randomly generated sample combinations, where samples were randomly divided into two groups consisting of n_A and n_B irrespective of their cell types, *i.e.*, tumor or normal cells. In this process, the random permutation method was applied 1000 times to produce a background distribution.

Distribution of the Fisher's ratios is symmetrical for the average values when two groups are different, whereas the average of the Fisher's ratio is close to 0 and the distribution takes positive value if two groups are not different. Therefore, the Fisher's ratio's distribution generated by 1000 random trials was adjusted by the distribution of a presumptive 2000 trials that was symmetrical to the Y axis, where the average Fisher's ratio is 0. Then, each gene was ranked according to a T-value for z-test between distributions of the true Fisher's ratio and background Fisher's. The T-value for the jth gene was calculated by following formula:

$$T_j = (F_{j\;avg.\;of\;true} - F_{j\;avg.\;of\;bg}) / (\sigma - f^F_{true}{}^2/n_{true} + \sigma - f^F_{bg}{}^2/n_{bg})^{0.5}$$

where $F_{j\;avg.\;of\;true}$ $F_{j\;avg.\;of\;bg}$ $\sigma - f^F_{true}{}^2$, n_{true}, $\sigma - f^F_{bg}{}^2$ and n_{bg} are the mean of Fisher's ratio, the mean background Fisher's ratio,
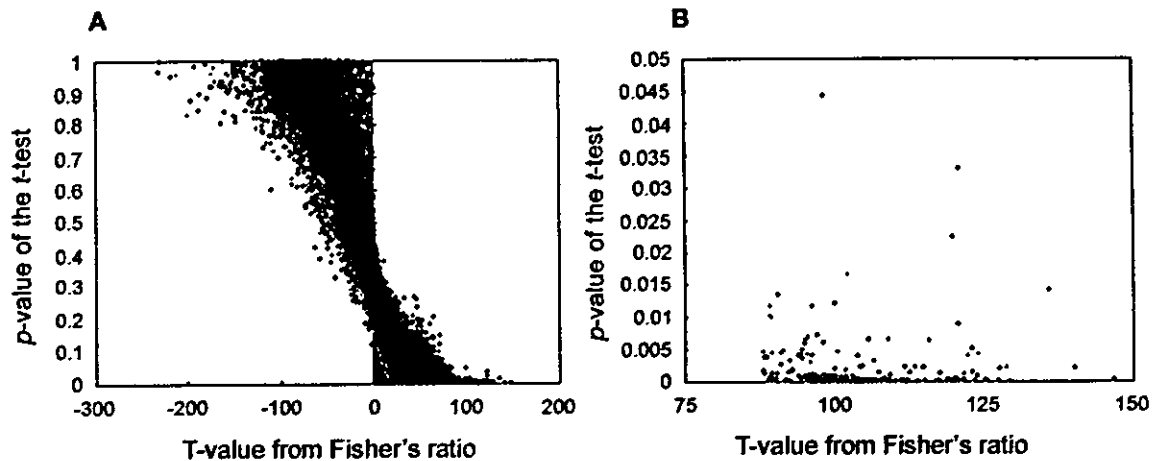
Figure 1. *T-values calculated from Fisher's ratio and p-values from Welch's t-test. T-values for each gene were calculated from Fisher's ratio and background Fisher's ratio and plotted along with p-values of Welch's t-test. A: Double plot of the T-values and p-values for all genes. B: Double plot of the T-values and p-values for the top 150 genes selected according to the T-values. Blue dots and red dots indicate genes selected from lung tissues and from pancreas tissues, respectively. All the top 150 genes selected by T-value show statistical significance (p<0.05) as shown in panel B.*

variance of true Fisher's ratio, the number of sample sets for calculating true Fisher's ratios, variance of background Fisher's ratios and the number of sample sets for calculating background Fisher's ratios. In addition, $\sigma\text{-}^{F}{}_{bg}$ was replaced by $(1000\text{-}1/2000\text{-}1)^{0.5} \times \sigma^{F}{}_{bg}$ for correction. The absolute value of T-values were not considered because $F_{j\ avg.\ of\ true} > F_{j\ avg.\ of\ bg}$ is important in this process. Finally, the significance of differences in the expression of the selected genes was validated by Welch's *t*-test, which is indicated as the *p*-value.

Gene clustering and Pearson's correlation analysis. Clustering was performed with a hierarchical clustering tool (7) after normalizing each gene expression and calculating the average distance. Pearson's correlation was calculated using Microsoft EXCEL. GeneSpring 5.0 (Silicon Genetics, CA, USA) was used for gene ontology classification .

Results

To profile the gene expressions of the two tumor types, laser-capture microdissection was used for the DNA microarray because lung tumor and pancreatic tumor tissues often contain large portions of stroma cells such as fibroblasts. For the comparison of gene expression profiles between tumor cells and corresponding normal tissues, we isolated cells from the normal epithelium of lung and pancreatic ducts. Total RNA was isolated from approximately 2,000 cells of 14 lung carcinomas, 9 normal lung epithelia, 13 pancreatic carcinomas and 13 normal epithelia of pancreatic ducts. Because the total RNA extracted from the dissected cells (20-100 ng) was not sufficient to generate cRNA for hybridization, it was amplified by twice repeating the synthesis of cDNA and cRNA.

To identify the genes whose expression was significantly different between tumor and normal cells, we calculated Fisher's ratios for various combinations of the sample sets. For lung tissues, we created 14 different sample sets consisting of 13 lung carcinomas and 9 different sample sets consisting of 8 normal lung epithelia. The average and standard deviation of the Fisher's ratios between tumor and normal from all 126 (14 x 9) combinations were calculated for each gene. To evaluate the distribution of the true Fisher's ratio, mean background Fisher's ratios were calculated from 1000 randomly-generated sample sets, which were further adjusted by the distribution of 2000 presumptive trials (see Materials and Methods). Then, the true Fisher's ratios for each gene were ranked in order of T-values for the z-test, that was determined with the true and background Fisher's ratios. The same analysis was performed with pancreatic carcinomas and normal epithelium of the pancreatic ducts, and the genes ranked based on the order of the T-values. Figure 1 shows a scattered plot of T-values and *p*-values determined by the Welch's *t*-test in each gene. In both lung carcinomas and pancreatic carcinomas, all of the top 150 genes ranked by this method showed *p*-values less than 0.05 (Figure 1 B).

When the lung tissue specimens were clustered with genes that were ranked in the top 150, tumor and normal samples were clearly separate; the same was also true for pancreatic tissue specimens (Figures 2 and 3). Among the top 150 ranked genes for lung or pancreatic tissues, many encode proteins responsible for the mitotic spindle assembly and/or chromosome segregation that function at G2-M transition. We therefore examined whether the expressions of genes

233

Figure 2. *Separation of tumor cells from normal cells by clustering with genes selected according to T-values in lung tissues. Lung carcinoma tumor and epithelium of normal tissues were clustered with the top 150 genes selected according to their T-values (A) and with the 11 genes that were commonly selected in both lung and pancreas tissues (B). Eight out of the 11 genes that were commonly selected in both lung and pancreas tissues are responsible for spindle and/or kinetochore. Note that the expression of the 8 genes was up-regulated in tumor cells compared with normal cells in lung.*
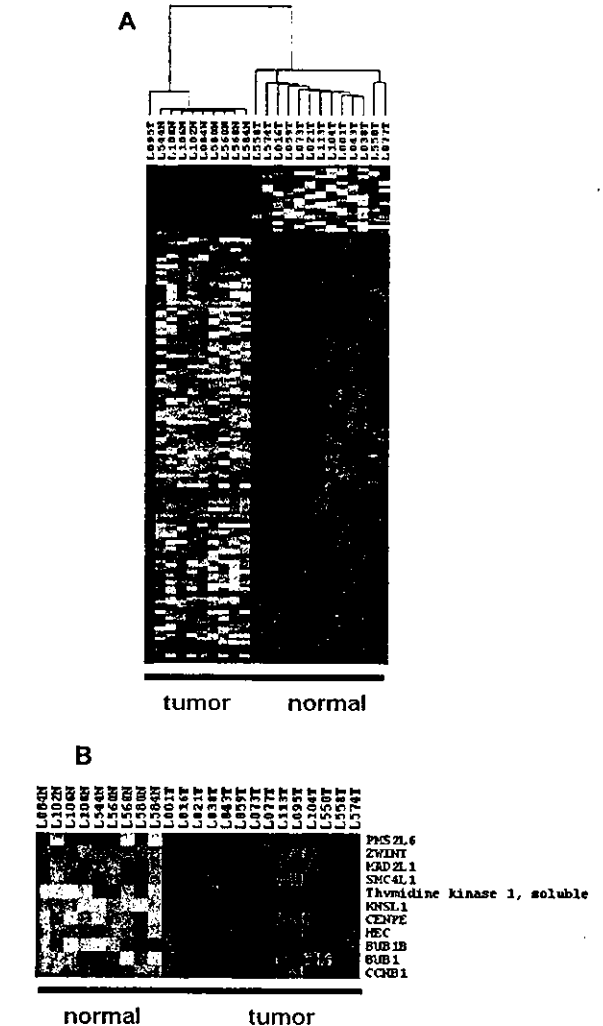
Figure 3. *Separation of tumor cells from normal cells by clustering with genes selected according to their T-values in pancreatic tissues. Pancreatic carcinoma (tumor) and pancreatic duct epithelium (normal) tissues were clustered with the top 150 genes selected according to their T-values (A) and with the 11 genes that were commonly selected in both lung and pancreas tissues (B). Eight out of the 11 genes that were commonly selected in both lung and pancreas tissues are responsible for spindle and/or kinetochore. Note that the expression of the 8 genes was up-regulated in tumor cells compared with normal cells in pancreas.*

involved in the spindle and kinetochore were different between tumor and normal cells in lung and pancreatic tissues. According to the classification of the genes based on annotation using the GeneSpring ontology, the Affymetrix U95A chip appeared to contain 42 probes for the spindle- and kinetochore-related genes. Clustering the lung or pancreatic tissues with the 42 genes also clearly distinguished tumor tissues from normal tissues (Figure 4). These results

indicate that one of the most significant differences in the gene expression profiles between tumor and normal tissues is the modulation of the expression of the genes for spindle, kinetochore and their related functions.

In an attempt to identify common changes in gene expression among tumors of different tissue types and stages, we looked for genes whose expression was altered in both lung carcinomas and pancreatic carcinomas. Among the top
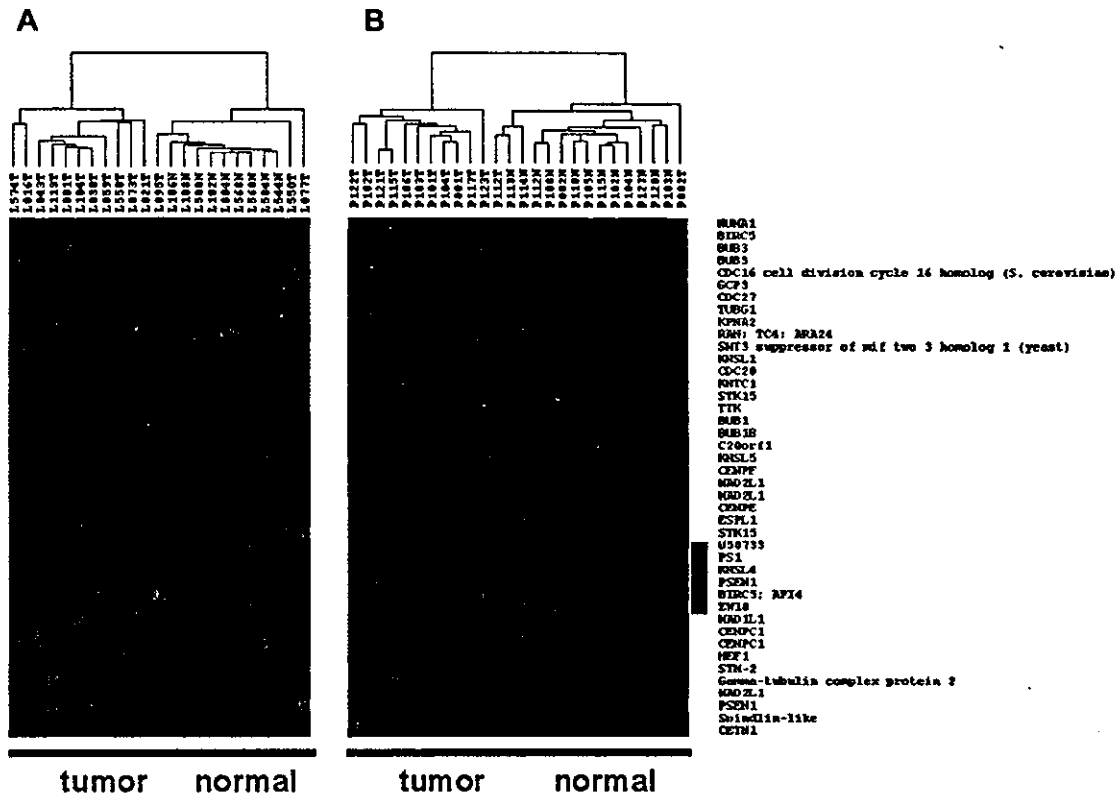
234

Figure 4. *Separation of tumor cells from normal cells by clustering with genes for kinetochore- and spindle-related genes. Tumor and normal tissues of lung (A) and pancreas (B) were clustered with 42 genes that are classified as kinetochore- and spindle-related genes. Kinetochore- and spindle-related genes in the probes of the Affymetrix GeneChip U95A ver.2 were selected based on the ontology classification of genes by GeneSpring. Expression patterns between tumor and normal cells of most of genes are similar in pancreas and lung, but those of genes with orange bars (U50733, PS1, KNSL4, PSEN1, BIRC5 and ZW10) show different patterns.*

150 ranked genes whose expression was significantly altered in lung carcinomas and pancreatic carcinomas as compared to their normal counterparts, 11 genes were found whose expression was up-regulated in both tumors: *MAD2L1, KNSL1, ZWINT, BUB1B, PMS2L6, CENPE, TK (thymidine kinase), HEC, SMC4L1, CCNB1* and *BUB1* (Figures 2B, 3B and Table I). Although PMS2L6 and TK are responsible for DNA mismatch repair and DNA synthesis, respectively (8, 9), other genes encode proteins for mitotic spindle assembly and/or chromosome segregation. *BUB1* (10), *BUB1B* (11, 12), *CENPE* (13) *HEC* (14) and *MAD2* (15-18) proteins serve as spindle checkpoints by inactivating the *CDC20* protein (19-21). We therefore asked whether the expression of *BUB1, BUB1B, CENPE, HEC,* or *MAD2L1* correlated with that of *CDC20*. As shown in Figure 5, expression of *CDC20* was also up-regulated in tumors compared to normal tissues, but it did not correlate well with the expression of the above 5 genes. However, there was a clear correlation

between the expression of *HEC* and that of *BUB1B* in both lung carcinomas and pancreatic carcinomas (Figure 5F). The search for genes whose expression correlated to that of *BUB1, BUB1B, CENPE, HEC,* or *MAD2L1* with a *p*-value less than 0.01, in both lung carcinomas and pancreatic carcinomas, yielded 40 genes. Among these 40 genes, 13 genes turned out to be responsible for the spindle and/or kinetochore, or chromosome segregation-related genes. As shown in Table II, the expression of *BUB1* correlated with that of *HSP90, HEC,* alpha-centractin, *CENPE* and topoisomerase truncated form, and that of HEC correlated with those of *TOPBP1, STK15, YES1* and *CCNB1.* Furthermore, there were clear correlations of the expression between *TTK* and *TOP2A,* between *MAD2L1* with *CENPF,* and between *MAD2L1* and a gene for kinesin-related protein. All of the genes described above encode proteins involved in spindle assembly and/or chromosome segregation at the metaphase to anaphase transition. Together, these

235

Table I. *Genes that were commonly identified in top 150 selected genes in lung and pancreas tissue samples.*

				lung				panc			
probe set	Common	Genbank	Map	N-average	T-average	T/N=	p-value of t-test	N-average	T-average	T/N=	p-value of t-test
37282_at	MAD2L1	AJ000186	4q27	16.7±16.2	150.5±119.5	9.0	0.00106	22.3±10.2	65.8±42.3	2.9	0.00307
40726_at	KNSL1	U37426	10q24.1	31.3±15.2	353.5±183.3	11.3	0.00002	70.4±28.7	192.3±89.1	2.7	0.00032
35995_at	ZWINT	AF067656	10q21-q22	162.2±43.8	1535.6±1018.0	9.5	0.00022	263.0±93.9	770.3±152.1	2.9	0.00000
35699_at	BUB1B	AF053306	15q15	87.6±37.9	407.1±207.3	4.6	0.00006	67.6±17.0	193.6±44.5	2.9	0.00000
32310_f_at	PMS2L6	AI341574	7q11-q22	89.5±31.6	272.0±121.9	3.0	0.00007	105.6±45.4	178.3±45.5	1.7	0.00043
37173_at	CENPE	Z15005	4q24-q25	7.0±3.5	62.1±34.6	8.9	0.00004	6.3±1.7	22.8±22.7	3.6	0.02226
41400_at	Thymidine kinase 1	K02581	16	172.9±62.9	645.0±283.2	3.7	0.00002	223.8±72.3	476.2±189.1	2.1	0.00040
40041_at	HEC	AF017790	18p11.31	91.3±24.6	737.1±457.6	8.1	0.00015	128.1±74.4	368.8±138.6	2.9	0.00003
34878_at	SMC4L1	AB019987	3q26.1	73.6±30.4	389.3±273.6	5.3	0.00083	51.5±22.2	135.4±86.2	2.6	0.00448
34736_at	CCNB1	M25753	5q12	20.8±13.4	399.6±246.3	19.2	0.00007	54.8±24.9	218.3±90.2	4.0	0.00002
41081_at	BUB1	AF053305	2q14	22.5±12.8	95.9±50.9	4.3	0.00011	19.5±9.9	52.7±14.9	2.7	0.00000

T/N: fold change from average.

Table II. *Genes whose expression correlated with that of sprindle checkpoint genes and are annotated as kinotochore, sprindle and/or cell cycle regulator.*

				lung				panc			
				R=		p-value		R=		p-value	
correlation with	probe set	name	Genbank	normal	tumor	normal	tumor	normal	tumor	normal	tumor
BUB1	33984_at	HSP90	M16660	0.20827	0.66632	0.59076	0.00927	0.27428	0.76149	0.36448	0.00249
BUB1B	40041_at	HEC	AF017790	0.17073	0.80793	0.66053	0.00047	0.32325	0.75760	0.28134	0.00270
BUB1B	40052_at	alpha-centractin	X82206	0.04522	0.66539	0.9C803	0.00940	0.17569	0.68711	0.56588	0.00947
CENPE	904_s_at	topisomerase truncated form	L47276	0.35131	0.75735	0.35390	0.00171	0.07661	0.82605	0.80356	0.00050
CENPE	572_at	TTK	M86699	0.26738	0.71506	0.48671	0.00405	0.15075	0.80071	0.62301	0.00101
CENPE	40145_at	TOP2A	AI375913	0.40864	0.71436	0.27484	0.00410	0.11770	0.76879	0.70176	0.00213
HEC	38834_at	TOPBP1	D87448	0.46506	0.85710	0.20716	0.00009	0.27504	0.69860	0.36310	0.00790
HEC	34852_g_at	STK15	AF011468	0.79709	0.82081	0.01010	0.00032	0.50624	0.72144	0.07753	0.00538
HEC	1674_at	YES1	M15990	0.39334	0.68805	0.29495	0.00652	0.05013	0.87856	0.87082	0.00008
HEC	34736_at	CCNB1	M25753	0.28043	0.67576	0.46483	0.00798	0.52419	0.73341	0.06594	0.00433
MAD2L1	1721_g_at	MAD2L1	U65410	0.20799	0.93691	0.59127	0.00000	0.73235	0.80665	0.00442	0.00086
MAD2L1	37302_at	CENPF	U30872	0.51337	0.81226	0.15750	0.00042	0.64759	0.90752	0.01671	0.00002
MAD2L1	38933_at	kinesin related protein	AL021366	0.14247	0.66756	0.71463	0.00909	0.53421	0.77461	0.06003	0.00018

Among 40 that were identified by the expression correlation analysis with spindle checkpoint genes, 13 genes that are annotated as kinetochore, spindle and/or cell cycle regulator are indicated.

results suggest that up-regulation of the expression of the genes for mitotic spindle and chromosome segregation is a common feature of tumor cells in at least lung and pancreatic cancers.

Discussion

We selected 150 genes whose expression was modulated in lung carcinomas or pancreatic carcinomas as compared to their normal counterparts, *i.e.* epithelium of lung and pancreatic ducts. To avoid the stroma cells from gene expression analysis, DNA microarray was performed with tumor cells and corresponding normal cells isolated by laser capture microdissection. Previous reports also compared the gene expression profiles of pancreatic adenocarcinomas with normal epithelium of ducts (22, 23). In this study, we looked for genes that were commonly up-regulated or down-regulated in different tumor types, and gene expression profiling was carried
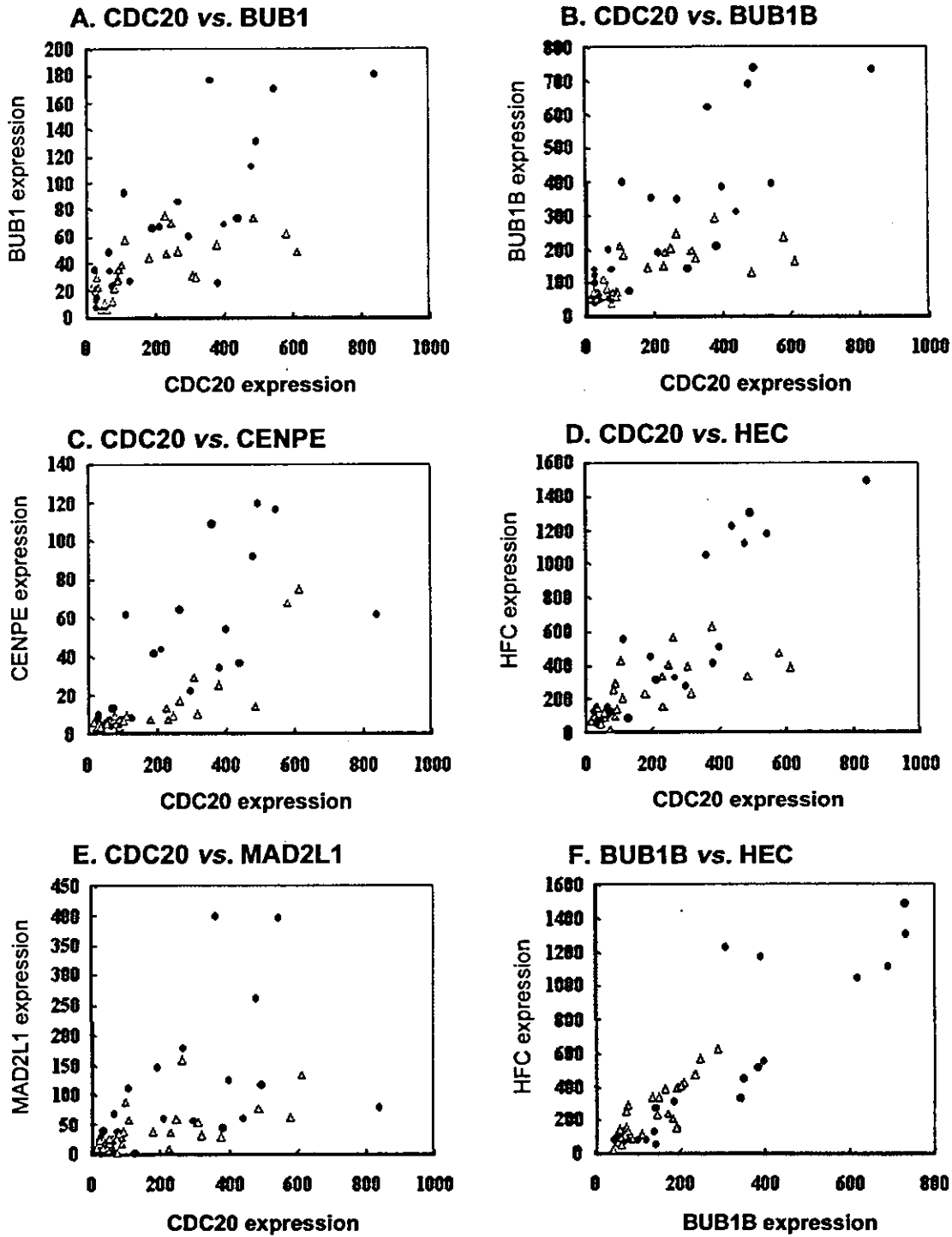
236

434

Figure 5. *Correlation of the expressions between CDC20 and spindle checkpoint genes. Correlations of the expression of the CDC20 and spindle checkpoint genes such as BUB1, BUB1B, CENPE, HEC and MAD2L1 were examined. The expression of CDC20 in each sample was plotted with that of BUB1 (A), BUB1B (B), CENPE (C), HEC (D) and MAD2L1 (E). Correlation of the expression between BUB1B and HEC is also indicated (F). Gene expression in tissue is indicated as follows: red circles, lung carcinomas; blue circles, normal lung epithelium; red triangles, pancreatic carcinomas; and blue triangles, epithelium of normal pancreatic ducts. Note that there is a positive correlation between the expression of BUB1B and HEC (F).*
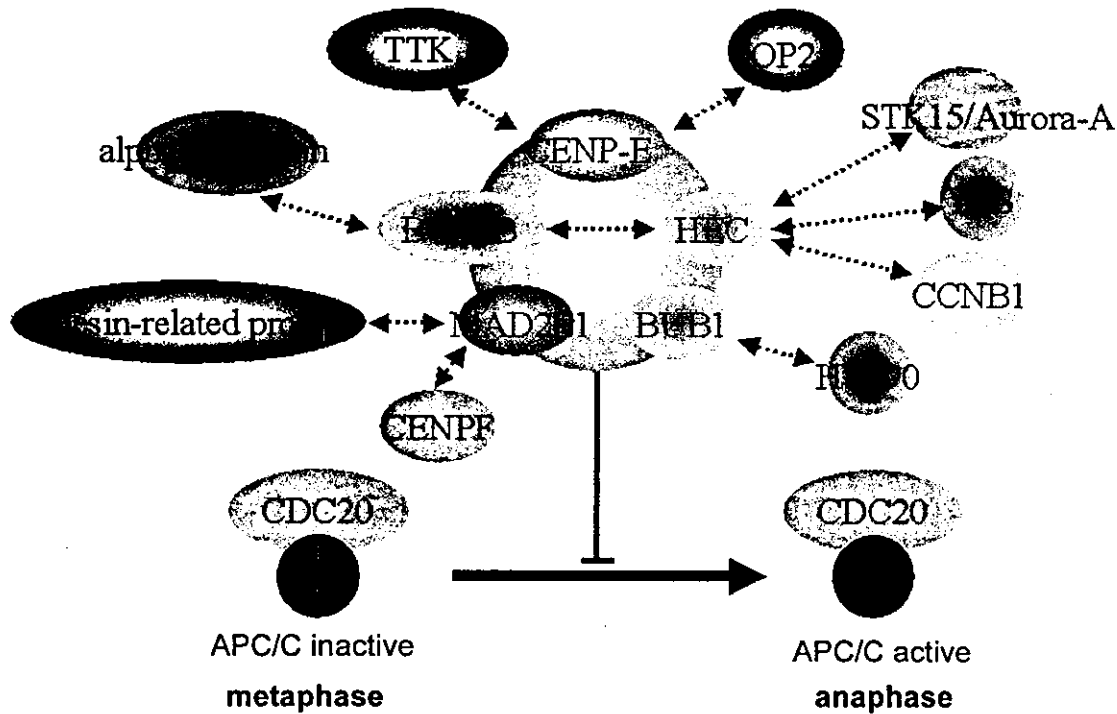
237

Figure 6. *Predicted expression network of spindle checkpoint genes, cell cycle regulators and kinetochore binding proteins in tumor cells. An expression network of the genes for spindle checkpoint, cell cycle regulation and kinetochore binding was predicted based on the gene expression profile and correlation analysis of the genes that are involved in spindle checkpoint. In lung and pancreatic tumor tissues, expression of spindle checkpoint genes was significantly up-regulated (center, in red) as compared to their normal counterparts. Up-regulation of the expression of spindle checkpoint genes will result in the suppression of the CDC20 activity that regulates anaphase promoting complex (APC/C) activity. The dotted blue arrows indicate a correlation of the expression in both lung carcinomas and pancreatic carcinomas.*

out with pancreatic carcinomas and lung carcinomas. Genes whose expression differed between tumor and corresponding normal tissues were ranked by T-values determined from the true Fisher's ratios and background Fisher's ratios, calculated from various combinations of the tumor and normal tissues. Validation by Welch's *t*-test revealed that differences between tumor and normal tissues in the expression of the top 150 genes ranked by T-values were considered to be statistically significant, because *p*-values were below 0.05. Performance of this screening procedure was reasonably high, because cluster analysis with the genes ranked top 150 in each tumor type clearly distinguish tumor from normal specimens. Genes ranked in the top 150 include many genes responsible for G2-M transition, especially for mitotic spindle assembly and chromosome segregation, strongly suggesting that one of the most remarkable features of tumor cells *in vivo* is the altered expression of genes involved in G2-M transition. In fact, cluster analysis with genes involved in mitotic spindle assembly and chromosome segregation also clearly distinguish tumor tissues from normal tissues in both lung and pancreas specimens.

Among the genes whose expression was significantly different in the tumor tissues as compared to their normal counterparts, 11 genes were commonly identified in two different tumor types with different tissue types and stages. Furthermore, 9 out of the 11 genes were found to be responsible for mitotic spindle assembly or chromosome segregation at the metaphase to anaphase transition, and the expression of all 9 genes were up-regulated in tumor cells as compared to their normal counterpart. Among these genes, *MAD2L1, BUB1, BUB1B, HEC* and *CENPE* encode spindle checkpoint proteins that are responsible for monitoring the attachment of microtubules to kinetochore. Furthermore, the expressions of other cell cycle and kinetochore-related genes such as *ZWINT, KNSL1, SMC4L1* and *CCNB1* also increased in both lung carcinomas and pancreatic carcinomas. *ZWINT* was originally identified as a gene for a protein that interacts with *ZW10*, whose defect caused aneuploidity in *Drosophila* and was shown to regulate anaphase onset in a tension-sensitive manner (24). *KNSL1* and *SMC4L1* encode a microtubule protein necessary for

mitotic spindle formation and a protein essential for mitotic chromosome condensation, respectively (25). The reason for the increased expression of the G2-M checkpoint genes in tumor tissues remains unknown, but the sensitivity and specificity of tumors to M-phase inhibitors such as taxanes, vinorelbine and epothilones may be attributable to an increased expression of G2-M checkpoint genes in tumor cells.

We applied Pearson's correlation in order to explore the expression network of spindle checkpoint genes. A search for genes whose expression correlated with that of *MAD2L1*, *BUB1*, *BUB1B*, *HEC*, or *CENPE* yielded 40 genes. Among these 40, 13 genes including *YES1* (26, 27), *CCNB1* (28, 29), *TOP2A* (and truncated form of topoisomerase) (30-32), *TOPBP1* (33), *STK15/Aurola A* (34), *TTK* (35), *Hsp90* (36) and alpha centractin (37) are involved in the metaphase to anaphase transition. The predicted gene expression network is summarized in Figure 6. The genes identified by the correlation analysis have not been reported as spindle checkpoint genes; however, several lines of evidence suggest that they are involved in kinetochore and/or spindle function. Both kinesin-related protein and alpha-centractin are thought to be responsible for kinetochore movement (37). CENPF shares a sequence homology with kinesins and localizes at the kinetochore plate to regulate kinetochore maturation (38). In addition, CENPF interacts with the CENPE (13), and CENPE also interacts with BUB1B (39). TTK, STK15 and YES all possess kinase activities and affect chromosome segregation. TTK, a human homologue of yeast MPS1, is required for the assembly of spindle checkpoint proteins (35). STK15/Aurora A kinase has been shown to be essential for chromosome segregation and centrosome functions (34). Furthermore, over-expression of STK15 in mammalian cells resulted in aneuploidy (34). YES, an src-related protein tyrosine kinase, is likely to be involved in mitotic progression because an inhibitor of this kinase interfered with spindle assembly (26, 27). HSP90 is a core centrosomal component and treatment of the cells with its specific inhibitor, geldanamycin, caused aberrant mitotic spindles (36). In *Drosophila*, the Cdc37/Hsp90 complex modulates a function of Aurora B kinase that is essential for chromosome segregation (40). TOP2A codes for topoisomerase that is necessary for the maintenance and segregation of the mitotic chromosomes (30, 32). Finally, CCNB is a cyclin responsible for the metaphase to anaphase transition (29). Thus, correlation analysis is a useful method to explore the functional networks of genes with mRNA expression profiles.

Acknowledgements

References

1 Ginsberg RJ, Vokes EE and Raben A: Non-small cell lung cancer. *In*: Cancer, Principles and Practice or Oncology (Devita VT Jr, Hellman S and Rosenberg SA, ed.), 5th edition, Lippincott-Raven, NewYork, pp. 858-911, 1997.

2 Evans DB, Abbruzzese JL and Rcih TA: Cancer of pancreas. *In*: Cancer, Principles and Practice or Oncology (Devita VT Jr, Hellman S and Rosenberg SA, ed.), 5th edition, Lippincott-Raven, NewYork, pp. 1054-1087, 1997.

3 Mohr S, Leikauf GD, Keith G and Rihn BH: Microarrays as cancer keys: an array of possibilities. J Clin Oncol *20*: 3165-75, 2002.

4 Guo QM: DNA microarray and cancer. Curr Opin Oncol *15*: 36-43, 2003.

5 Iizuka N, Oka M, Yamada-Okabe H, Mori N, Tamesa T, Okada T, Takemoto N, Tangoku A, Hamada K, Nakayama H, Miyamoto T, Uchimura S and Hamamoto Y: Comparison of gene expression profiles between hepatitis B virus- and hepatitis C virus-infected hepatocellular carcinoma by oligonucleotide microarray data on the basis of a supervised learning method. Cancer Res *62*: 3939-3944, 2002.

6 Iizuka N, Oka M, Yamada-Okabe H, Nishida M, Maeda Y, Mori N, Takao T, Tamesa T, Tangoku A, Tabuchi H, Hamada K, Nakayama H, Ishitsuka H, Miyamoto T, Hirabayashi A, Uchimura S and Hamamoto Y: Oligonucleotide microarray for prediction of early intrahepatic recurrence of hepatocellular carcinoma after curative resection. Lancet *361*: 923-929, 2003.

7 Eisen MB, Spellman PT, Brown PO and Botstein D: Cluster analysis and display of genome-wide expression patterns. Proc Natl Acad Sci USA *95*: 14863-14868, 1998.

8 Risinger JI, Umar A, Barrett JC and Kunkel TA: A hPMS2 mutant cell line is defective in strand-specific mismatch repair. J Biol Chem *270*: 18183-18186, 1995.

9 Guarne A, Junop MS and Yang W: Structure and function of the N-terminal 40 kDa fragment of human PMS2: a monomeric GHL ATPase. EMBO J *20*: 5521-5531, 2001.

10 Warren CD, Brady DM, Johnston RC, Hanna JS, Hardwick KG and Spencer FA: Distinct chromosome segregation roles for spindle checkpoint proteins. Mol Boil Cell *13*: 3029-3041, 2002.

11 Fang G: Checkpoint protein BubR1 acts synergistically with Mad2 to inhibit anaphase-promoting complex. Mol Biol Cell *13*: 755-766, 2002.

12 Chen RH: BubR1 is essential for kinetochore localization of other spindle checkpoint proteins and its phosphorylation requires Mad1. J Cell Biol *158*: 487-496, 2002.

13 Abrieu A, Kahana JA, Wood KW and Cleveland DW: CENP-E as an essential component of the mitotic checkpoint *in vitro*. Cell *102*: 817-826, 2000.

14 Martin-Lluesma S, Stucke VM and Nigg EA: Role of HEC1 in spindle checkpoint signaling and kinetochore recruitment of Mad1/Mad2. Science *297*: 2267-2270, 2002.

15 Gorbsky GJ, Chen RH and Murray AW: Microinjection of antibody to Mad2 protein into mammalian cells in mitosis induces premature anaphase. J Cell Biol *141*: 1193-1205, 1998.

16 Shah JV and Cleveland DW: Waiting for anaphase: Mad2 and the spindle assembly checkpoint. Cell *103*: 997-1000, 2000.

17 Zhang Y and Lees E: Identification of an overlapping binding domain on Cdc20 for Mad2 and anaphase-promoting complex: model for spindle checkpoint regulation. Mol Cell Biol *21*: 5190-5199, 2001.

239

18 Skoufias DA, Andreassen PR, Lacroix FB, Wilson L and Margolis RL: Mammalian mad2 and bub1/bubR1 recognize distinct spindle-attachment and kinetochore-tension checkpoints. Proc Natl Acad Sci USA *98*: 4492-4497, 2001.

19 Yu H: Regulation of APC-Cdc20 by the spindle checkpoint. Curr Opin Cell Biol *14*: 706-714, 2002.

20 Cleveland DW, Mao Y and Sullivan KF: Centromeres and kinetochores: from epigenetics to mitotic checkpoint signaling. Cell *112*: 407-421, 2003.

21 Musacchio A and Hardwick KG: The spindle checkpoint: structural insights into dynamic signaling. Nat Rev Mol Cell Biol *3*: 731-741, 2002.

22 Crnogorac-Jurcevic T, Efthimiou E, Nielsen T, Loader J, Terris B, Gordon S, Baron A, Scarpa A and Lemoine NR: Expression profiling of microdissected pancreatic adenocarcinomas. Oncogene *21*: 4587-4594, 2002.

23 Nakamura T, Furukawa Y, Nakagawa H, Tsunoda T, Ohigashi H, Murata K, Ishikawa O, Ohgaki K, Kashimura N, Miyamoto M, Hirano S, Kondo S, Katoh H, Nakamura Y and Katagiri T: Genome-wide cDNA microarray analysis of gene expression profiles in epithelial cells selected for purity by laser microdissection. Oncogene *23*: 1-16, 2004.

24 Starr DA, Saffery R, Li Z, Simpson AE, Choo KH, Yen TJ and Goldberg ML: HZwint-1, a novel human kinetochore component that interacts with HZW10. J Cell Sci *113*: 1939-1950, 2000.

25 Hirano T: The ABCs of SMC proteins: two-armed ATPase for chromosome condensation, cohesion, and repair. Genes Develop *16*: 399-414, 2002.

26 Roche S, Fumagalli S and Courtneidge SA: Requirement for Src family protein tyrosine kinases in G2 for fibroblast cell division. Science *269*: 1567-1569, 1995.

27 Moasser MM, Srethapakdi M, Sachar KS, Kraker AJ and Rosen N: Inhibition of Src kinases by a selective tyrosine kinase inhibitor causes mitotic arrest. Cancer Res *59*: 6145-6152, 1999.

28 Chang CD, Xu N, Kathy Q and Luo KQ: Degradation of Cyclin B is required for the onset of anaphase in mammalian cells. J Biol Chem *278*: 37865-37873, 2003.

29 Wang Q, Moyret-Lalle C, Couzon F, Surbiguet-Clippe C, Saurin J-C, Lorca T, Navarro C and Puisieux A: Alterations of anaphase-promoting complex genes in human colon cancer cells. Oncogene *22*: 1486-1490, 2003.

30 Tavormina PA, Come MG, Hudson JR, Mo YY, Beck WT and Gorbsky GJ: Rapid exchange of mammalian topoisomerase II alpha at kinetochores and chromosome arms in mitosis. J Cell Biol *158*: 23-29, 2002.

31 Null AP, Hudson J and Gorbsky GJ: Both alpha and beta isoforms of mammalian DNA topoisomerase II associate with chromosomes in mitosis. Cell Growth Differ *13*: 325-333, 2002.

32 Kallio M and Lahdetie J: Effects of the DNA topoisomerase II inhibitor merbarone in male mouse meiotic divisions *in vivo*: cell cycle arrest and induction of aneuploidy. Environ Mol Mutagen *29*: 16-27, 1997.

33 Yamamoto R R, Axton JM, Yamamoto Y, Saunders RD, Glover DM and Henderson DS: The *Drosophila* mus101 gene, which links DNA repair, replication and condensation of heterochromatin in mitosis, encodes a protein with seven BRCA1 C-terminus domains. Genetics *156*: 711-721, 2000.

34 Anand S, Penrhyn-Lowe S and Venkitaraman AR: AURORA-A amplification overrides the mitotic spindle assembly checkpoint, inducing resistance to Taxol. Cancer Cell *3*: 51-62, 2003.

35 Stucke VM, Sillje HHW, Arnaud L and Nigg EA: Human Mps1 kinase is required for the spindle assembly checkpoint but not for centrosome duplication. EMBO J *21*: 1723-1732, 2002.

36 Clark IB and Meyer DI: Overexpression of normal and mutant Arp1 alpha (centractin) differentially affects microtuble organization during mitosis and interphase. J Cell Science *112*: 3507-3518, 1999.

37 Lange BMH, Rebollo E, Herold A and Gonzalez C: Cdc37 is essential for chromosome segregation and cytokinesis in higher eukaryotes. EMBO J *21*: 5364-5374, 2002.

38 Choo AKH: Centromere proteins of higher eukaryotes. *In*: The Centromere (Choo AKH, ed.). Oxford University Press (NewYork, N.Y.) pp.144-253.

39 Chan GKT, Schaar BT and Yen TJ: Characterization of the kinetochore binding domain of CENP-E reveals interaction with the kinetochore proteins CENP-F and hBUBR1. J Cell Biol *143*: 49-63, 1998.

40 Lange BMH, Bachi A, Wilm M and Gonzalez C: Hsp90 is a core centrosomal component and is required at different stages of the centrosome cycle in *Drosophila* and vertebrates. EMBO J *19*: 1252-1262, 2000.